

Model-Based Reconstruction for Joint Estimation of T_1 , R_2^* and B_0 Field Maps Using Single-Shot Inversion-Recovery Multi-Echo Radial FLASH *

Xiaoqing Wang^{†1}, Nick Scholand², Zhengguo Tan³, Daniel Mackner², Vitali Telezki⁴, Moritz Blumenthal², Philip Schaten², and Martin Uecker^{2,3,4,5,6}

¹Department of Radiology, Harvard Medical School, Boston, Massachusetts, USA

²Institute of Biomedical Imaging, Graz University of Technology, Austria

³Department of Artificial Intelligence in Biomedical Engineering, University of Erlangen-Nuremberg, Germany

⁴German Centre for Cardiovascular Research (DZHK), Partner Site Göttingen, Göttingen, Germany

⁵Institute for Diagnostic and Interventional Radiology, University Medical Center Göttingen, Göttingen, Germany

⁶Cluster of Excellence "Multiscale Bioimaging: from Molecular Machines to Networks of Excitable Cells" (MBExC), University of Goettingen, Germany

⁷BioTechMed-Graz, Graz, Austria

February 9, 2024

Abstract

Purpose: To develop a model-based nonlinear reconstruction for simultaneous water-specific T_1 , R_2^* , B_0 field and/or fat fraction (FF) mapping using single-shot inversion-recovery (IR) multi-echo radial FLASH.

Methods: The proposed model-based reconstruction jointly estimates water-specific T_1 , R_2^* , B_0 field and/or FF maps, as well as a set of coil sensitivities directly from k -space obtained with a single-shot IR multi-echo

*Part of this work has been presented at the ISMRM Workshop on Data Sampling and Image Reconstruction, Sedona, 2023. Xiaoqing Wang and Nick Scholand contributed equally to this work.

[†]Xiaoqing Wang, Boston Children's Hospital, Harvard Medical School, 300 Longwood Avenue, 02115, Boston, MA, USA. xiaoqingwang2010@gmail.com

radial FLASH sequence using blip gradients across echoes. Joint sparsity constraints are exploited on multiple quantitative maps to improve precision. Validations are performed on numerical and NIST phantoms and with in vivo studies of the human brain and liver at 3 T.

Results: Numerical phantom studies demonstrate the effects of fat signals in T_1 estimation and confirm good quantitative accuracy of the proposed method for all parameter maps. NIST phantom results confirm good quantitative T_1 and R_2^* accuracy in comparison to Cartesian references. Apart from good quantitative accuracy and precision for multiple parameter maps, in vivo studies show improved image details utilizing the proposed joint estimation. The proposed method can achieve simultaneous water-specific T_1 , R_2^* , B_0 field and/or FF mapping for brain ($0.81 \times 0.81 \times 5 \text{ mm}^3$) and liver ($1.6 \times 1.6 \times 6 \text{ mm}^3$) imaging within four seconds.

Conclusion: The proposed model-based nonlinear reconstruction, in combination with a single-shot IR multi-echo radial FLASH acquisition, enables joint estimation of accurate water-specific T_1 , R_2^* , B_0 field and/or FF maps within four seconds. The present work is of potential value for specific clinical applications.

Keywords: model-based reconstruction, water-specified T_1 mapping, R_2^* mapping, B_0 estimation, fat fraction, multi-echo radial FLASH

1 Introduction

Quantitative T_1 and R_2^* mapping are of increasing interest in a number of clinical use cases [1]. While T_1 relaxation time can be efficiently measured with an inversion-recovery (IR) Look-Locker (LL) technique [2, 3, 4], R_2^* mapping is accomplished by the multi-echo FLASH readout [5]. The latter can also be utilized for water-fat separation [6, 7, 8, 9, 10] based on the Dixon method [11]. Conventionally, IR LL T_1 mapping employs a single-echo readout with the shortest TE to minimize off-resonance effects [3]. Recent advances extend the single-echo readout to two or three echoes, which enables water-specific T_1 mapping and reduces errors caused by fat components [12, 13]. Meanwhile, the latest efforts in MR fingerprinting, multitasking and others empower simultaneous water-specific T_1 , T_2 , R_2^* mapping by extending single-echo to multi-echo readout [14, 15, 16, 17, 18, 19, 20, 21].

To enable efficient quantitative imaging, sparsity and subspace-constraints along the parameter dimensions have been developed to accelerate parameter mapping in general [22, 23, 24, 25, 26]. Following image reconstruction, quantitative parameter maps can be obtained by performing a nonlinear fitting/matching of the reconstructed images to the underlying physical model. Among them, subspace-constrained reconstruction is one of the state-of-the-art approaches [23, 27]. It approximates the MR signal evolution by a linear subspace. Because the number of subspace coefficients is usually much smaller than that of contrast-weighted images, the subspace method is very efficient. The inversion-recovery part can be effectively represented by only a few subspace coefficients, but the phase accumulation in long multi-echo readout caused by field inhomogeneities requires a large number of coefficients approximating

the multi-echo FLASH signal [28, 29, 30]. This makes the subspace approach less efficient in the case of combined inversion-recovery multi-echo acquisition.

Nonlinear model-based reconstruction is an alternative approach for efficient quantitative MRI [31, 32, 33, 34, 35, 36, 30, 37]. It reconstructs the underlying physical parameter maps directly from k -space, bypassing the intermediate steps of image reconstruction and pixelwise fitting/matching. Recently, this kind of method was extended to efficiently reconstruct water, fat and R_2^* maps from an undersampled multi-echo FLASH acquisition [7, 9]. Our developments further enable an additional B_0 estimation [38]. However, current model-based reconstruction can not be directly applied to the IR multi-echo data due to the contrast changes in the course of inversion recovery, in contrary to the steady-state conditions [7, 9, 38]. Existing approaches [12, 13] instead utilize separate steps, i.e., first extract the multi-echo part at longer inversion time (approximating the steady-state condition) for water-fat separation, and subsequently utilize the estimated parameter maps from the first step for water-fat separated T_1 estimation. Although this simplifies the reconstruction, the separate use of data may result in sub-optimal solutions as not all available data is utilized and the correlation between quantitative maps (such as T_1 and R_2^*) is not fully exploited.

Inspired by the above advances, in this work, we aim to develop a fully nonlinear model-based reconstruction method for joint water-specific T_1 , R_2^* , B_0 and/or fat fraction (FF) mapping using the IR multi-echo radial FLASH acquisition. In particular, we first combine a single-shot inversion recovery sequence with a multi-echo radial FLASH readout. We further incorporate blip gradients across echoes to enable an efficient k -space coverage. Second, after modeling the underlying physical signal, we formulate parameter estimation as a nonlinear inverse problem, i.e., to jointly estimate water T_1 , R_2^* , B_0 and/or FF maps directly from the acquired k -space data. Thus, the present work is capable of exploiting all available information for a joint estimation. Furthermore, similar to [39] and [40], we are able to make use of smooth regularization on the B_0 maps and joint sparsity constraints on the other parameter maps to improve the reconstruction.

2 Theory

Sequence Design

The single-shot IR multi-echo radial FLASH sequence is demonstrated in the Supporting Information Figure S1. It starts with a non-selective inversion pulse, followed by a continuous multi-echo radial FLASH readout. To allow for efficient k -space coverage, radial spokes are designed to rotate along the echo dimension using blip gradients [41]. The distribution of spokes is designed in a way that radial spokes from several TRs (e.g., 9) and all echoes are equally distributed in one k -space [41], with an angle $\theta_{l,m} = 2\pi/(N_E \cdot N_S) \cdot [(l-1) \cdot N_E + m - 1]$ for the l th TR and the m th echo. N_E and N_S are the number of echoes and

shots (TRs) per k -space frame, respectively. Spokes acquired in consecutive k -space frame are rotated by a small golden-angle ($\approx 68.75^\circ$) with respect to the previous one [42] to enable a complementary coverage of k -space.

Signal Model

Based on the signal equations of IR Look-Locker and multi-echo gradient echo acquisitions, the signal evolution for the above process can be described by

$$\begin{aligned} S_{\text{TI}_n, \text{TE}_m} = & \left[W_{ss} - (W_{ss} + W_0) \cdot \exp(-\text{TI}_n \cdot R_{1,W}^*) \right. \\ & + (F_{ss} - (F_{ss} + F_0) \cdot \exp(-\text{TI}_n \cdot R_{1,F}^*)) \cdot z_m \left. \right] \\ & \cdot \exp(\text{TE}_m \cdot i2\pi f_{B_0}) \cdot \exp(-\text{TE}_m \cdot R_2^*). \end{aligned} \quad (1)$$

Where $(W_{ss}, W_0, R_{1,W}^*)^T$ are the steady-state signal, the equilibrium-state signal and the effective T_1 relaxation rate for water, and $(F_{ss}, F_0, R_{1,F}^*)^T$ represent the same components for fat. z_m is the 6-peak fat spectrum [43], f_{B_0} represents the field inhomogeneity and R_2^* is the effective relaxation rate. TI_n and TE_m denote the n th inversion time and m th echo time, respectively. The sought quantitative parameters in equation (1) are then $x_p = (W_{ss}, W_0, R_{1,W}^*, F_{ss}, F_0, R_{1,F}^*, f_{B_0}, R_2^*)^T$. In some cases, such as for the National Institute of Standards and Technology (NIST) phantom [44], where no fat component is present, the above signal equation (1) can be simplified to

$$\begin{aligned} S_{\text{TI}_n, \text{TE}_m} = & \left[W_{ss} - (W_{ss} + W_0) \cdot \exp(-\text{TI}_n \cdot R_{1,W}^*) \right] \\ & \cdot \exp(\text{TE}_m \cdot i2\pi f_{B_0}) \cdot \exp(-\text{TE}_m \cdot R_2^*). \end{aligned} \quad (2)$$

The corresponding sought quantitative parameters become $x_p = (W_{ss}, W_0, R_{1,W}^*, f_{B_0}, R_2^*)^T$.

Model-Based Reconstruction

Combining the above physical models with the parallel imaging equation [45, 46], we construct a nonlinear forward operator F , which maps the unknowns in Equation (1) and the unknown coil sensitivities C to the acquired multi-channel data y at TI_n and TE_m , i.e.,

$$F : x \mapsto y = \mathcal{P}\mathcal{F}C \cdot S_{\text{TI}_n, \text{TE}_m}(x_p). \quad (3)$$

Here, \mathcal{P} is the sampling pattern and \mathcal{F} is the Fourier transform. By setting $x_c = (c_1, \dots, c_k, \dots, c_K)^T$ (with c_k the individual k th coil sensitivity map), the vector of unknowns in Equation (3) is $x = (x_p, x_c)^T$. The estimation of x is then formulated as an optimization problem, i.e.,

$$\hat{x} = \underset{x \in D}{\text{argmin}} \sum_{\text{TI}} \sum_{\text{TE}} \|\mathcal{P}\mathcal{F}C \cdot S_{\text{TI}_n, \text{TE}_m}(x) - Y_{\text{TI}_n, \text{TE}_m}\|_2^2 + R(x). \quad (4)$$

Here, D is a convex set, ensuring non-negativity of all relaxation rates. $R(\cdot)$ is the regularization term for both parameter maps and coil sensitivity maps. In particular, we use joint ℓ_1 -Wavelet sparsity constraint [40] on $(W_{ss}, W_0, R_{1,W}^*, F_{ss}, F_0, R_{1,F}^*, R_2^*)^T$ or $(W_{ss}, W_0, R_{1,W}^*, R_2^*)^T$ to exploit sparsity and correlations between maps and Sobolev regularization on the f_{B_0} map [38] and the coil sensitivity maps [46] to enforce smoothness. The above optimization problem is solved by IRGNM-FISTA [40] using the Berkeley Advanced Reconstruction Toolbox (BART) [47]. More details for IRGNM-FISTA can be found in Ref. [40]. Additionally, the derivative of the nonlinear operator and the adjoint of the derivative which are needed in the algorithm can be found in Appendix.

3 Methods

Numerical Simulations

To evaluate the accuracy of the proposed nonlinear model-based approach, a digital phantom with ten circular tubes and a background was simulated. The numerical phantom models has water T_1 ranging from 200 ms to 2000 ms for tubes, and 3000 ms for the background, and fat T_1 ranging from 300 ms to 400 ms for tubes, and 300 ms for the background. R_2^* for the tubes is ranging from 5 s^{-1} to 100 s^{-1} , and 5 s^{-1} for the background, and off-resonance is ranging from -50 Hz to 50 Hz for the tubes, and -50 Hz for the background. The fat fraction (FF) was set to be constant (20%) for all tubes and the background. The k -space data was derived from the analytical Fourier representation of ellipses with an array of eight circular receiver coils surrounding the phantom. The simulation employed an IR multi-echo radial FLASH sequence as described above with a base resolution of 192 pixels covering a field of view of 128 mm, $\text{TR}/\text{TE}_1/\delta\text{TE}_1 = 12.7/1.6/1.6 \text{ ms}$, 7 echoes, flip angle 6° , and total acquisition time of 4 s. To study the effects of the fat signal on the accuracy of the T_1 map, simulations with IR single-echo FLASH sequences, utilizing $\text{TR}/\text{TE} = 5/1.15 \text{ ms}$ (out-of-phase) and $\text{TR}/\text{TE} = 5/2.3 \text{ ms}$ (in-phase), were also conducted. Finally, complex white Gaussian noise was added to the simulated k -spaces.

Data Acquisition

All MRI experiments were performed on a Magnetom Skyra 3T (Siemens Healthineers, Erlangen, Germany). Validation was first performed on the T_2 spheres of a NIST phantom (model version 130) [44]. Phantom and brain studies were conducted with a 20-channel head/neck coil, whereas abdominal scans were performed with a combined thorax and spine coil with 26 channels. Three subjects (3 male, 29 ± 7 years old) without known illness were recruited and scans were performed after written informed consent was obtained. The acquisition parameters for phantom and brain were: matrix size = 256×256 , slice thickness = 5 mm, 7 echoes with $\text{TR} = 15.6 \text{ ms}$, $\text{TE}_{1-7} = 2.26/4.2/6.14/8.08/10.10/12.1/14.1 \text{ ms}$, $\text{FA} = 6^\circ$, bandwidth = 810 Hz/pixel, and 300 RF excitations with 2100 ra-

dial acquired spokes for all echoes. The FOV was $220 \times 220 \text{ mm}^2$ for the phantom and $208 \times 208 \text{ mm}^2$ for the brain. Acquisition parameters for abdomen were: FOV = $320 \times 320 \text{ mm}^2$, matrix size = 200×200 , slice thickness = 6 mm, 7 echoes with TR = 10.6 ms, TE₁₋₇ = 1.49/2.61/3.73/4.85/5.97/7.09/8.21 ms, FA = 6°, bandwidth = 1320 Hz/pixel and 360 RF excitations with 2520 radial acquired spokes for all echoes. Abdominal experiments were accomplished during a brief breathhold. All acquisition parameters are summarized in the Supporting Information Table S1.

For reference, a gold-standard T_1 mapping [48] was performed on the NIST phantom using the IR spin-echo method with 7 TIs (TI = 30, 280, 530, 780, 1030, 1280, 1530 ms). Reference phantom and brain R_2^* and B_0 maps were taken from the Cartesian multi-echo FLASH acquisitions provided by the vendor with TEs = (2.54, 4.92, 7.38, 9.84, 12.30, 14.76, 17.22 ms) and TEs = (4.92, 7.38 ms), respectively. For liver studies, reference R_2^* , fat fraction (FF) and B_0 maps were estimated using a recently developed model-based reconstruction of the steady-state multi-echo data [38]. The steady-state data was extracted from the last 120 excitations of the same IR LL multi-echo experiment with a prolonged acquisition of 6 seconds and corresponding to around 1.2 s at the end. In-vivo T_1 references were using the previously developed single-shot T_1 mapping method [40] with single-echo readout.

Iterative Reconstruction

The proposed model-based reconstruction algorithm was implemented in C and CUDA using the nonlinear operator and optimization framework of BART [49]. Both 5-parameter and 8-parameter model-based reconstructions were implemented. While the former was used for the NIST phantom study, the latter was used for reconstructing all the other data sets. Similar to [38], to prevent the phase modulation caused by phase wrapping along the echoes, the B_0 map was initialized from a three-point model-based water/fat separation [41] and the R_2^* map was initialized to zero. All the other parameters were initialized to one. Furthermore, since T_1 , fat signals, R_2^* and B_0 have different physical units, they may have differently scaled gradients during optimization, affecting the convergence speed of the proposed method. To balance the relative gradients, three additional scaling variables were introduced: L_F , $L_{R_2^*}$ and L_{B_0} , resulting in transformed variables $\hat{F}_{ss} = F_{ss}/L_F$, $\hat{F}_0 = F_0/L_F$, $\hat{R}_2^* = R_2^*/L_{R_2^*}$ and $\hat{B}_0 = B_0/L_{B_0}$ which are used in the optimization. Note here that both F_{ss} and F_0 are scaled by L_F according to Equation (2). Practically, L_F was set to be 0.5, $L_{R_2^*}$ and L_{B_0} were set to be in the order of [0.04, 0.1] after examining the L2-norm of the gradient of each map during iterations manually. This setting resulted in stable reconstructions for all cases tested, as shown in the convergence curves in the Supporting Information Figure S2.

All data processing was conducted offline with BART. Following gradient delay correction using RING [50], the acquired inversion-prepared multi-coil multi-echo data was compressed to eight virtual coils via principal component

analysis [51]. Similar to the previous studies [52, 53], the multicoil radial data were initially gridded onto a Cartesian grid, and all subsequent iterations were then performed using FFT-based convolutions with the point-spread function [54]. To enhance computational efficiency, six spokes were combined into one k -space frame for all data sets. With the above settings, all computations were executed on a GPU with 48 GB of memory (RTX A6000, NVIDIA, Santa Clara, CA), resulting in a computation time of 10 - 20 minutes per dataset.

Quantitative Analysis

All quantitative results are reported as mean \pm standard deviation (SD). Regions-of-interest (ROIs) were drawn into the quantitative maps using the arrayShow [55] tool implemented in MATLAB (MathWorks, Natick, MA). Bland–Altman analyses were used to compare ROI-based mean quantitative values between reference and the proposed model-based reconstruction. Scan-rescan test were carried out to assess repeatability of this method. Moreover, the coefficient of variation ($\text{CoV} = \text{SD}_{\text{ROI}}/\text{Mean}_{\text{ROI}} \times 100\%$) was used for the evaluation of quantitative precision.

4 Results

Numerical Simulation

We first validated the proposed model-based reconstruction on a numerical phantom, which provides a wide range of ground-truth quantitative values in the presence of noise. Figure 1 (A) shows the estimated water-specific T_1 , fat T_1 , fat fraction (FF), R_2^* and B_0 maps. Figure 1 (B) shows a comparison of the corresponding ROI-analyzed quantitative values to the ground truth. The low mean differences (2 ± 3 ms, -2 ± 9 ms, 0.9 ± 1.2 %, -0.2 ± 0.1 s $^{-1}$ and 0.0 ± 0.04 Hz for water-specific T_1 , fat T_1 , fat fraction (FF), R_2^* and B_0 maps, respectively) indicate that a good quantitative accuracy has been achieved. Figure 1 (C) shows the estimated in-phase and out-of-phase T_1 maps using the single-echo model-based reconstruction [40] and their comparison to the ground truth. If the fat component is present but not incorporated into the signal model, the mean T_1 difference is lower than the ground truth (underestimation) in the in-phase case and higher than the ground truth (overestimation) in the out-of-phase case. Figure 1 (D) shows the effects of the amount of fat signals on single-echo T_1 estimation of three selected tubes. As expected, the relative T_1 error increases with a larger fat fraction. Note that for T_1 values smaller than the fat T_1 (i.e., 200 ms vs. 300 ms), the difference exhibits an opposite sign to the larger ones.

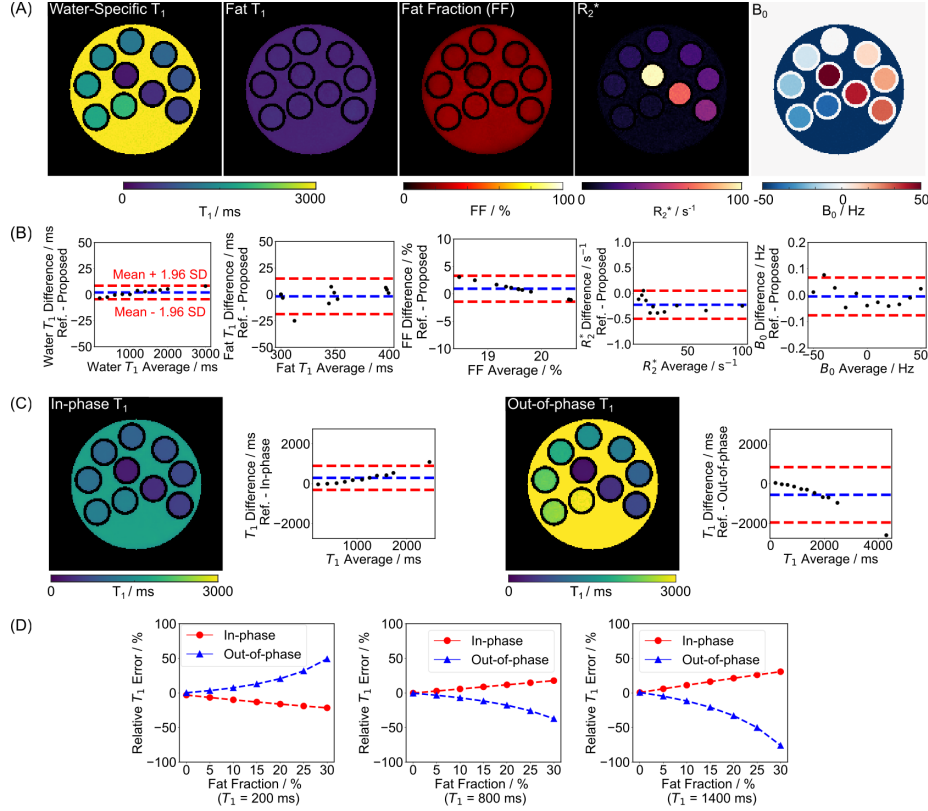


Figure 1: (A) Model-based estimated water-specific T_1 , fat T_1 , fat fraction (FF), R_2^* and B_0 maps from a single-shot multi-echo radial acquisition of a numerical phantom. (B) Bland–Altman plots comparing the ROI-analyzed mean quantitative values to the ground truth. The mean differences are 2 ± 3 ms, -2 ± 9 ms, 0.9 ± 1.2 %, -0.2 ± 0.1 s^{-1} and 0.0 ± 0.04 Hz for water-specific T_1 , fat T_1 , FF, R_2^* and B_0 maps, respectively. (C) In-phase (TE = 2.3 ms) and out-of-phase (TE = 1.15 ms) T_1 maps estimated using the single-echo model-based reconstruction [40]. The mean differences are 292 ± 309 ms and -558 ± 713 ms for in-phase and out-of-phase T_1 s, respectively. Similar to (A) and (B), the fat fraction (FF) is 20% here. (D) The effects of fat signals on single-echo T_1 estimation of three selected tubes. The more fat components, the larger the relative T_1 errors. Note that for T_1 smaller than the fat T_1 (i.e., 200 ms vs. 300 ms), the difference exhibits an opposite sign to the larger ones.

Phantom Validation

Figure 2 (A) shows the estimated NIST phantom T_1 , R_2^* and B_0 maps using the proposed method and reference methods. Note that the 5-parameter model was used here. Visual inspection reveals good agreement between the proposed

method and references for the selected tubes (T_1 range of [200, 3000] ms and R_2^* range of [10, 200] s^{-1} (equivalent to T_2^* range of [5, 100] ms)). Moreover, the proposed method reduces background noise in the R_2^* map due to the direct regularization on the R_2^* map. The good correspondence is confirmed quantitatively in the ROI-analyzed values that are shown in Figure 2 (B) with relatively small mean differences of 31 ± 21 ms and 0.3 ± 1.4 s^{-1} for T_1 and R_2^* , respectively.

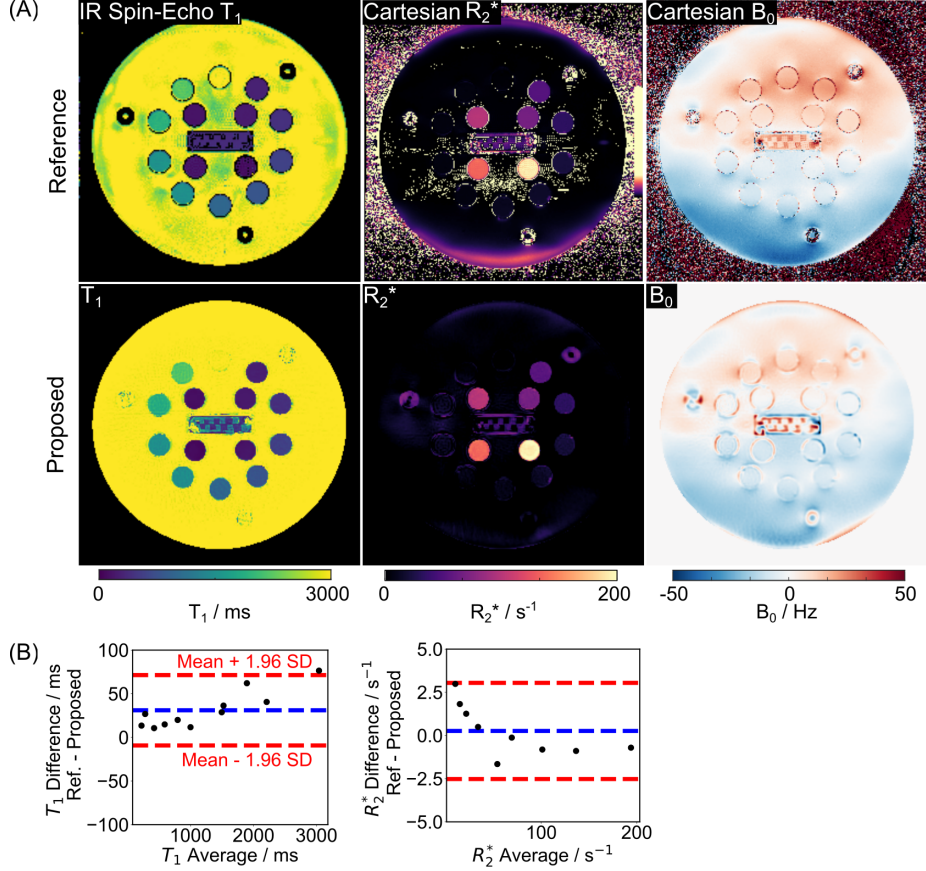


Figure 2: (A) Model-based estimated T_1 , R_2^* and B_0 maps and their comparison to the Cartesian references of the NIST phantom. (B) Bland-Altman plots comparing the ROI-analyzed mean quantitative T_1 and R_2^* values to the references. The mean differences are 31 ± 21 ms and 0.3 ± 1.4 s^{-1} for T_1 and R_2^* maps, respectively. Please note that only tubes with a T_1 range of [200, 3000] ms and R_2^* range of [10, 200] s^{-1} (equivalent to T_2^* range of [5, 100] ms) are displayed.

In Vivo Studies

The Supporting Information Figure S3 (A) demonstrates the effect of the regularization parameter on brain water-specific T_1 and R_2^* maps. Low values of the regularization parameter result in increased noise, while high values lead to improved precision (CoV values from left to right: $4.3 \pm 0.5\%$, $3.5 \pm 0.5\%$, $3.1 \pm 0.7\%$ and $2.8 \pm 0.9\%$ for T_1 and $10.0 \pm 2.3\%$, $6.8 \pm 1.3\%$, $5.2 \pm 1.0\%$ and $4.3 \pm 1.0\%$ for R_2^*), but it also causes blurring. A value of 0.004 was chosen to balance noise reduction and preservation of image details for the brain reconstruction. Similarly, the regularization parameter was set to be 0.007 for the abdominal reconstructions, as shown in the Supporting Information Figure S3 (B).

With the above settings, Figure 3 (A) compares model-based reconstructed brain quantitative parameter maps to the references. Apart from variations in fluid and fat regions, the estimated quantitative maps are visually comparable to the references. The magnified view of the T_1 maps highlights improved image details (black arrow) through the proposed joint estimation and demonstrates the removal of fat signal from the water-specific T_1 map (white arrow). Supporting Information Figure S4 (A) illustrates the corresponding jointly estimated brain water (W_{ss}) and fat (F_{ss}) images. Furthermore, the proposed method exhibits fewer distortion effects on the R_2^* map compared to the reference method (black arrow). The Bland-Altman plot of ROI-analyzed values in Figure 3 (B) reveals good agreement between the proposed method and the references. The mean R_2^* difference is $-0.1 \pm 1.4 \text{ s}^{-1}$, and the mean T_1 difference is $-16 \pm 8 \text{ ms}$. The latter indicates slightly higher water-specific T_1 values by the proposed method compared to those estimated from the single-shot IR single-echo acquisition.

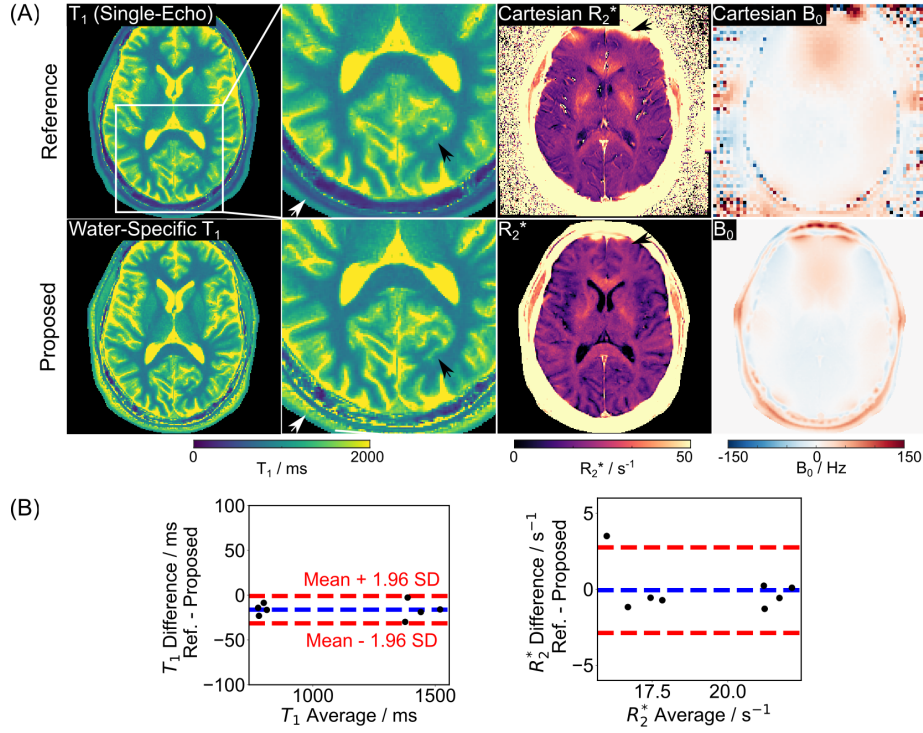


Figure 3: (A) Model-based reconstructed brain water-specific T_1 , its enlarged region, R_2^* and B_0 maps and their comparison to the references. The white arrow on the T_1 map indicates fat signal removal, while the black arrow highlights better preserved structural details with joint estimation. The black arrow on the R_2^* maps reflects reduced distortion artifacts achieved by the proposed method. (B) Bland–Altman plots comparing the ROI-analyzed mean quantitative water-specific T_1 and R_2^* values to the references. The mean differences are -16 ± 8 ms and $-0.1 \pm 1.4 s^{-1}$ for water-specific T_1 and R_2^* maps, respectively.

Figure 4 (A) displays two repetitive brain water-specific T_1 , R_2^* , and B_0 maps generated using the proposed method for two subjects. The minor visual differences between repetitive scans demonstrate good intra-subject repeatability. Quantitative confirmation in Figure 4 (B) via the Bland–Altman plot reveals small mean differences of 4 ± 11 ms and $0.1 \pm 0.5 s^{-1}$ for water-specific T_1 and R_2^* , respectively.

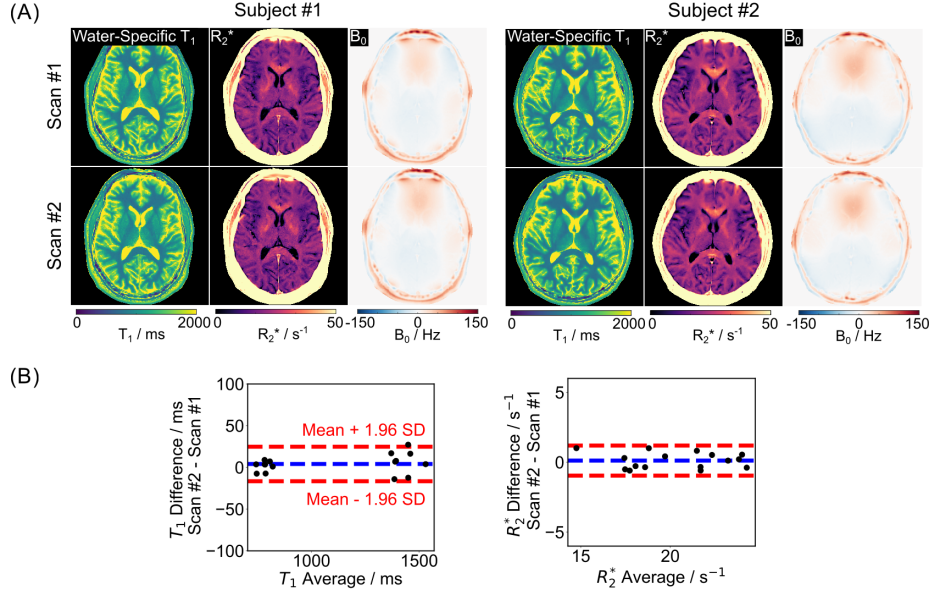


Figure 4: (A) Model-based reconstructed brain water-specific T_1 , R_2^* and B_0 maps for two repetitive scans and two subjects. (B) Bland-Altman plots comparing the ROI-analyzed mean quantitative water-specific T_1 and R_2^* values for two repetitive scans and two subjects. The mean differences are 4 ± 11 ms and 0.1 ± 0.5 s^{-1} for T_1 and R_2^* maps, respectively.

Figure 5 (A) presents model-based reconstructed liver water-specific T_1 , R_2^* , fat fraction, and B_0 maps using the proposed method and reference methods for one subject. Despite slight differences in breathing conditions between the two scans, quantitative maps are comparable. Similar to the brain case, the proposed joint estimation enhances spatial delineation of image details, particularly in the R_2^* map (white arrows), and eliminates fat signal in the water-specific T_1 map (white arrow). Supporting Information Figure S4 (B) includes the corresponding jointly estimated liver water (W_{ss}) and fat (F_{ss}) images. The quantitative comparison in Figure 5 (B) reveals good agreement with mean differences of -0.6 ± 3 s^{-1} for R_2^* , -0.3 ± 1.0 % for fat fraction (FF), and 12 ± 21 ms for water-specific T_1 . Again, the latter reflects slight differences (higher in this case) in water-specific T_1 values by the proposed method compared to those estimated from the single-shot IR single-echo acquisition. Additionally, the Supporting Information Figure S5 shows the reconstructed quantitative maps for the second scan. Despite differences in the B_0 maps to the first scan, which are likely caused by breathing [41], all other quantitative maps show good visual agreement. The quantitative comparison in Figure 5 (C) demonstrates small mean differences, with mean differences of 0.6 ± 6 ms, -2.5 ± 3.5 s^{-1} , and 0.2 ± 0.8 % for water-specific T_1 , R_2^* , and fat fraction, respectively, indicating good repeatability of the proposed method.

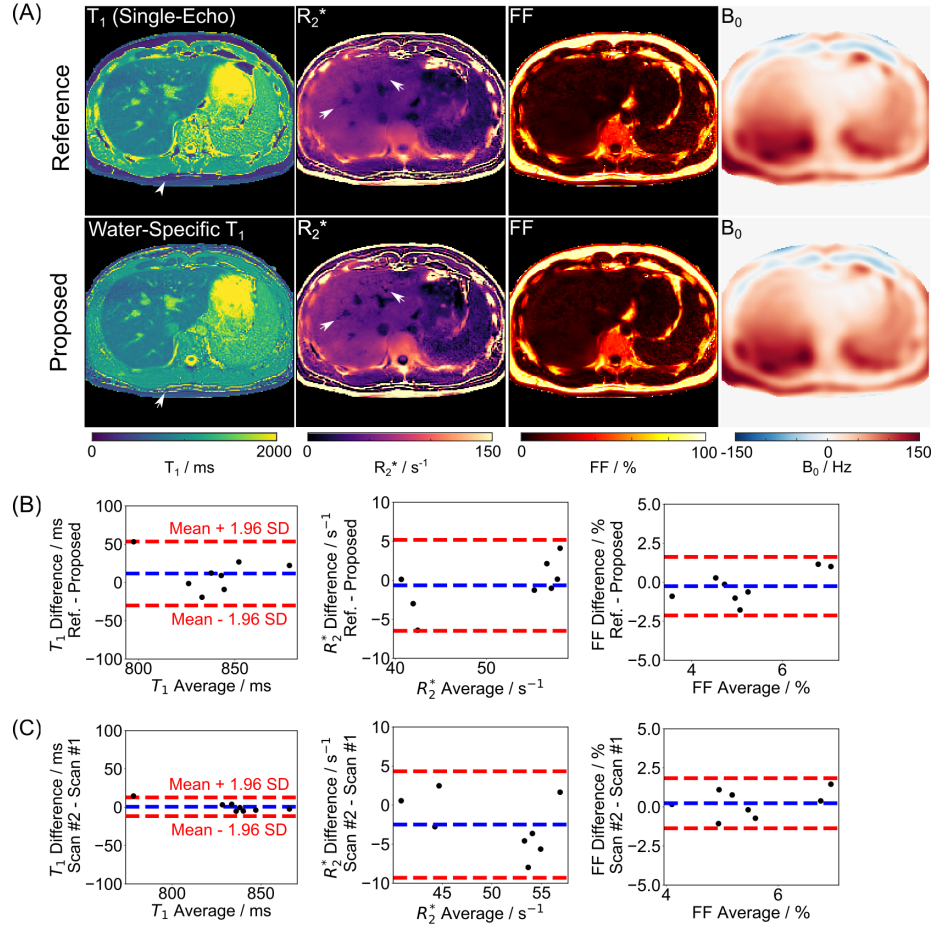


Figure 5: (A) Model-based reconstructed liver water-specific T_1 , R_2^* , fat fraction and B_0 maps and their comparison to the references. The white arrow on the T_1 map indicates the removal of fat signal, while the white arrows on the R_2^* maps reflect improved structure details achieved with joint estimation. (B) Bland-Altman plots comparing the ROI-analyzed mean quantitative water-specific T_1 , R_2^* and fat fraction values to the references. The mean differences are 12 ± 21 ms, -0.6 ± 3 s^{-1} and -0.3 ± 1.0 % for water-specific T_1 , R_2^* and FF maps, respectively. (C) Bland-Altman plots comparing ROI-analyzed mean quantitative values for two repetitive scans of the same subject. The mean differences are 0.6 ± 6 ms, -2.5 ± 3.5 s^{-1} and $0.2 \pm 0.8\%$ for water-specific T_1 , R_2^* and FF maps, respectively. Quantitative maps for scan #2 can be found in the Supporting Information Figure S5.

5 Discussion

In this work, we investigated a joint water-specific T_1 , R_2^* , B_0 and FF mapping technique using single-shot IR multi-echo radial FLASH acquisition and nonlinear calibrationless model-based reconstruction. The proposed method models the underlying physical MR signal and formulates parameter estimation directly from all acquired data as a nonlinear inverse problem. This formulation allows the use of all complementary k -space information to determine the underlying quantitative maps. It also enables the use of joint sparsity constraints for multiple quantitative maps to further improve precision. Validation studies on a numerical phantom, the NIST phantom, brain and abdominal studies have not only demonstrated good quantitative accuracy, precision and repeatability, but also illustrated improved image details.

The enhanced image details may mainly result from leveraging all available information obtained through the IR multi-echo acquisition. In our current brain studies, for instance, utilizing 300 RF excitations and 7 echoes, a total of 2100 distinct spokes are exploited for the joint parameter estimation. This total number of spokes is more than that of the IR single-echo case [40], using around 975 spokes (with $TR = 4.1$ ms) for T_1 estimation. For the abdominal case, while the steady state has 840 (120×7) distinct spokes, the proposed method uses 2520 (360×7) different spokes from the entire inversion recovery for joint estimation.

The present work is situated within the ongoing investigation of rapid confounder-corrected T_1 mapping and joint multi-parameter mapping [12, 13, 14, 15, 16, 18, 17, 19, 21, 56, 57]. It has been reported that T_1 accuracy is affected by the presence of fat [58, 12, 13, 16, 21]. In line with previous findings, our simulation results confirm that, if fat is present but not modeled, T_1 values that are larger than fat T_1 are underestimated in the in-phase case and overestimated in the out-of-phase case. The relative T_1 estimation error increases with a higher fat fraction. Moreover, our simulation shows vice-versa estimation results for T_1 that are smaller than the fat T_1 . However, when the fat component is incorporated in the signal model, accurate T_1 can be determined using the proposed joint estimation. Our model-based brain and liver results have shown a similar trend. I.e., the water-specific brain T_1 is slightly higher than the single-echo case ($TE = 2.36$ ms, close to the in-phase condition) and liver T_1 is slightly lower than the single-echo case ($TE = 1.49$ ms, close to the out-of-phase condition).

As a technical development, the main limitation of the current study is the small sample size, and that no patient studies have been conducted. Evaluating the approach on a larger cohort, including both volunteers and patients, especially those with fatty liver disease and/or iron overload, would be of great interest and will be the subject of future work. The proposed model-based reconstruction is very general and can be applied to 3D imaging as well. Although the focus of the study has been on 2D imaging with a efficient single-shot acquisition, future research, integrating the proposed model-based reconstruction with techniques such as simultaneous multi-slice excitation [59] or stack-of-stars acquisition [12, 38], holds significant promise as it could enable efficient multiple

parameter mapping of the entire brain and/or liver.

6 Conclusion

The proposed model-based nonlinear reconstruction, in combination of a single-shot IR multi-echo radial FLASH acquisition, enables a joint estimation of accurate water-specific T_1 , R_2^* , B_0 , and/or FF maps with good precision and repeatability. The present work is of potential value for specific clinical applications.

7 Open Research

7.1 Data Availability Statement

In the spirit of reproducible research, code to reproduce the reconstruction and analysis will be available on <https://github.com/mrirecon/moba-irme>. The raw k -space data, all ROIs to reproduce the quantitative values and other relevant files used in this study can be downloaded from <https://doi.org/10.5281/zenodo.10529421>.

8 Acknowledgements

We thank Dr. Li Feng from New York University for the inspiring discussions.

A Appendix

Derivative and Adjoint Derivatives of the Operators

$$DF(x) \begin{pmatrix} dW_{ss} \\ dW_0 \\ dR_{1,w}^* \\ dF_{ss} \\ dF_0 \\ dR_{1,F}^* \\ df_{B_0} \\ dR_2^* \\ dc_1 \\ \vdots \\ dc_K \end{pmatrix} = \begin{pmatrix} \mathcal{P}_{1,1}\mathcal{F}\left\{c_1 \cdot \left(\frac{\partial S_{1,1}}{\partial W_{ss}}dW_{ss} + \frac{\partial S_{1,1}}{\partial W_0}dW_0 + \frac{\partial S_{1,1}}{\partial R_{1,w}^*}dR_{1,w}^* + \frac{\partial S_{1,1}}{\partial F_{ss}}dF_{ss} + \frac{\partial S_{1,1}}{\partial F_0}dF_0 + \frac{\partial S_{1,1}}{\partial R_{1,F}^*}dR_{1,F}^* + \frac{\partial S_{1,1}}{\partial f_{B_0}}df_{B_0} + \frac{\partial S_{1,1}}{\partial R_2^*}dR_2^*\right) + S_{1,1} \cdot dc_1\right\} \\ \vdots \\ \mathcal{P}_{n,m}\mathcal{F}\left\{c_1 \cdot \left(\frac{\partial S_{n,m}}{\partial W_{ss}}dW_{ss} + \frac{\partial S_{n,m}}{\partial W_0}dW_0 + \frac{\partial S_{n,m}}{\partial R_{1,w}^*}dR_{1,w}^* + \frac{\partial S_{1,1}}{\partial F_{ss}}dF_{ss} + \frac{\partial S_{1,1}}{\partial F_0}dF_0 + \frac{\partial S_{n,m}}{\partial R_{1,F}^*}dR_{1,F}^* + \frac{\partial S_{n,m}}{\partial f_{B_0}}df_{B_0} + \frac{\partial S_{n,m}}{\partial R_2^*}dR_2^*\right) + S_{n,m} \cdot dc_1\right\} \\ \vdots \\ \mathcal{P}_{n,m}\mathcal{F}\left\{c_K \cdot \left(\frac{\partial S_{n,m}}{\partial W_{ss}}dW_{ss} + \frac{\partial S_{n,m}}{\partial W_0}dW_0 + \frac{\partial S_{n,m}}{\partial R_{1,w}^*}dR_{1,w}^* + \frac{\partial S_{1,1}}{\partial F_{ss}}dF_{ss} + \frac{\partial S_{1,1}}{\partial F_0}dF_0 + \frac{\partial S_{n,m}}{\partial R_{1,F}^*}dR_{1,F}^* + \frac{\partial S_{n,m}}{\partial f_{B_0}}df_{B_0} + \frac{\partial S_{n,m}}{\partial R_2^*}dR_2^*\right) + S_{n,m} \cdot dc_K\right\} \\ \vdots \\ \mathcal{P}_{N,M}\mathcal{F}\left\{c_K \cdot \left(\frac{\partial S_{N,M}}{\partial W_{ss}}dW_{ss} + \frac{\partial S_{N,M}}{\partial W_0}dW_0 + \frac{\partial S_{N,M}}{\partial R_{1,w}^*}dR_{1,w}^* + \frac{\partial S_{N,M}}{\partial F_{ss}}dF_{ss} + \frac{\partial S_{N,M}}{\partial F_0}dF_0 + \frac{\partial S_{1,1}}{\partial R_{1,F}^*}dR_{1,F}^* + \frac{\partial S_{N,M}}{\partial f_{B_0}}df_{B_0} + \frac{\partial S_{N,M}}{\partial R_2^*}dR_2^*\right) + S_{N,M} \cdot dc_K\right\} \end{pmatrix}$$

and the adjoint is

$$\begin{pmatrix} dW_{ss} \\ dW_0 \\ dR_{1,w}^* \\ dF_{ss} \\ dF_0 \\ dR_{1,w}^* \\ df_{B_0} \\ dR_2^* \\ dc_1 \\ \vdots \\ dc_K \end{pmatrix} = DF^H(x) \begin{pmatrix} y_{1,1,1} \\ \vdots \\ y_{K,1,1} \\ y_{1,2,1} \\ \vdots \\ y_{K,N,M} \end{pmatrix} = \begin{pmatrix} \sum_{k=1}^K \sum_{n=1}^N \sum_{m=1}^M \left(\overline{\frac{\partial S_{n,m}}{\partial W_{ss}}} \cdot \overline{c_k} \cdot \mathcal{F}^{-1}\{\mathcal{P}_{n,m}y_{k,n,m}\} \right) \\ \vdots \\ \sum_{k=1}^K \sum_{n=1}^N \sum_{m=1}^M \left(\overline{\frac{\partial S_{n,m}}{\partial F_{ss}}} \cdot \overline{c_k} \cdot \mathcal{F}^{-1}\{\mathcal{P}_{n,m}y_{k,n,m}\} \right) \\ \vdots \\ \sum_{k=1}^K \sum_{n=1}^N \sum_{m=1}^M \left(\overline{\frac{\partial S_{n,m}}{\partial R_2^*}} \cdot \overline{c_k} \cdot \mathcal{F}^{-1}\{\mathcal{P}_{n,m}y_{k,n,m}\} \right) \\ \sum_{n=1}^N \sum_{m=1}^M \left(\overline{S_{n,m}} \cdot \mathcal{F}^{-1}\{\mathcal{P}_{n,m}y_{1,n,m}\} \right) \\ \vdots \\ \sum_{n=1}^N \sum_{m=1}^M \left(\overline{S_{n,m}} \cdot \mathcal{F}^{-1}\{\mathcal{P}_{n,m}y_{K,n,m}\} \right) \end{pmatrix}$$

with partial derivatives

$$\begin{aligned}
\frac{\partial S_{n,m}}{\partial W_{ss}} &= (1 - \exp(-\text{TI}_n \cdot R_{1,W}^*)) \cdot Z \\
\frac{\partial S_{n,m}}{\partial W_0} &= -\exp(-\text{TI}_n \cdot R_{1,W}^*) \cdot Z \\
\frac{\partial S_{n,m}}{\partial R_{1,w}^*} &= \text{TI}_n \cdot (W_{ss} + W_0) \cdot \exp(-\text{TI}_n \cdot R_{1,W}^*) \cdot Z \\
\frac{\partial S_{n,m}}{\partial F_{ss}} &= (1 - \exp(-\text{TI}_n \cdot R_{1,F}^*)) \cdot z_m \cdot Z \\
\frac{\partial S_{n,m}}{\partial F_0} &= -\exp(-\text{TI}_n \cdot R_{1,F}^*) \cdot z_m \cdot Z \\
\frac{\partial S_{n,m}}{\partial R_{1,F}^*} &= \text{TI}_n \cdot (F_{ss} + F_0) \cdot \exp(-\text{TI}_n \cdot R_{1,F}^*) \cdot z_m \cdot Z \\
\frac{\partial S_{n,m}}{\partial f_{B_0}} &= i2\pi \cdot \text{TE}_m \cdot S_{n,m} \\
\frac{\partial S_{n,m}}{\partial R_2^*} &= -\text{TE}_m \cdot S_{n,m}
\end{aligned}$$

where $Z = \exp(\text{TE}_m \cdot i2\pi f_{B_0}) \cdot \exp(-\text{TE}_m \cdot R_2^*)$, $S_{n,m}$ is the signal model in equation (1) and $\bar{\cdot}$ denotes pointwise complex conjugation. The 5-parameter ones can be derived by removing the fat parts from the above equations.

References

- [1] MargaretCheng HL, Stikov N, Ghugre NR, Wright GA. Practical medical applications of quantitative MR relaxometry. J. Magn. Reson. Imaging 2012; 36:805–824.
- [2] Look DC, Locker DR. Time saving in measurement of NMR and EPR relaxation times. Rev. Sci. Instrum. 1970; 41:250–251.
- [3] Deichmann R, Haase A. Quantification of T1 values by SNAPSHOT-FLASH NMR imaging. J. Magn. Reson. (1969) 1992; 96:608–612.
- [4] Messroghli DR, Radjenovic A, Kozerke S, Higgins DM, Sivananthan MU, Ridgway JP. Modified Look-Locker Inversion recovery (MOLLI) for high-resolution T1 mapping of the heart. Magn. Reson. Med. 2004; 52:141–146.
- [5] Frahm J, Haase A, Matthaei D. Rapid NMR imaging of dynamic processes using the FLASH technique. Magn. Reson. Med. 1986; 3:321–327.
- [6] Hernando D, Haldar J, Sutton B, Ma J, Kellman P, Liang ZP. Joint estimation of water/fat images and field inhomogeneity map. Magn. Reson. Med. 2008; 59:571–580.

- [7] Benkert T, Feng L, Sodickson DK, Chandarana H, Block KT. Free-breathing volumetric fat/water separation by combining radial sampling, compressed sensing, and parallel imaging. *Magn. Reson. Med.* 2017; 78:565–576.
- [8] Armstrong T, Dregely I, Stemmer A, Han F, Natsuaki Y, Sung K, Wu HH. Free-breathing liver fat quantification using a multiecho 3D stack-of-radial technique. *Magn. Reson. Med.* 2018; 79:370–382.
- [9] Schneider M, Benkert T, Solomon E, Nickel D, Fenchel M, Kiefer B, Maier A, Chandarana H, Block KT. Free-breathing fat and R_2^* quantification in the liver using a stack-of-stars multi-echo acquisition with respiratory-resolved model-based reconstruction. *Magn. Reson. Med.* 2020; 84:2592–2605.
- [10] Mayer J, Blaszczyk E, Cipriani A, Ferrazzi G, SchulzMenger J, Schaeffter T, Kolbitsch C. Cardio-respiratory motion-corrected 3D cardiac water-fat MRI using model-based image reconstruction. *Magn. Reson. Med.* 2022; 88:1561–1574.
- [11] Dixon WT. Simple proton spectroscopic imaging. *Radiology* 1984; 153:189–194.
- [12] Feng L, Liu F, Soultanidis G, Liu C, Benkert T, Block KT, Fayad ZA, Yang Y. Magnetization-prepared GRASP MRI for rapid 3D T1 mapping and fat/water-separated T1 mapping. *Magn. Reson. Med.* 2021; 86:97–114.
- [13] Li Z, Mathew M, Syed AB, Feng L, Brunsing R, Pauly JM, Vasanawala SS. Rapid fat–water separated T1 mapping using a single-shot radial inversion-recovery spoiled gradient recalled pulse sequence. *NMR Biomed.* 2022; 35:e4803.
- [14] Jaubert O, Arrieta C, Cruz G, Bustin A, Schneider T, Georgiopoulos G, Masci PG, SingLong C, Botnar RM, Prieto C. Multi-parametric liver tissue characterization using MR fingerprinting: Simultaneous T1, T2, T2*, and fat fraction mapping. *Magn. Reson. Med.* 2020; 84:2625–2635.
- [15] Hermann I, Kellman P, Demirel OB, Akçakaya M, Schad LR, Weingärtner S. Free-breathing simultaneous T1, T2, and T2* quantification in the myocardium. *Magn. Reson. Med.* 2021; 86:1226–1240.
- [16] Wang N, Cao T, Han F, Xie Y, Zhong X, Ma S, Kwan A, Fan Z, Han H, Bi X et al. Free-breathing multitasking multi-echo MRI for whole-liver water-specific T1, proton density fat fraction, and R_2^* quantification. *Magn. Reson. Med.* 2022; 87:120–137.
- [17] Cao T, Ma S, Wang N, Gharabaghi S, Xie Y, Fan Z, Hogg E, Wu C, Han F, Tagliati M et al. Three-dimensional simultaneous brain mapping of T1, T2, T2* and magnetic susceptibility with MR Multitasking. *Magn. Reson. Med.* 2022; 87:1375–1389.

- [18] Velasco C, Cruz G, Jaubert O, Lavin B, Botnar RM, Prieto C. Simultaneous comprehensive liver T1, T2, T1 ρ , and fat fraction characterization with MR fingerprinting. *Magn. Reson. Med.* 2022; 87:1980–1991.
- [19] Lima da Cruz GJ, Velasco C, Lavin B, Jaubert O, Botnar RM, Prieto C. Myocardial T1, T2, T2*, and fat fraction quantification via low-rank motion-corrected cardiac MR fingerprinting. *Magn. Reson. Med.* 2022; DOI: <https://doi.org/10.1002/mrm.29171>.
- [20] Wang F, Dong Z, Reese TG, Rosen B, Wald LL, Setsompop K. 3D Echo Planar Time-resolved Imaging (3D-EPTI) for ultrafast multi-parametric quantitative MRI. *NeuroImage* 2022; 250:118963.
- [21] Roberts NT, Tamada D, Muslu Y, Hernando D, Reeder SB. Confounder-corrected T1 mapping in the liver through simultaneous estimation of T1, PDFF, R2*, and B1+ in a single breath-hold acquisition. *Magn. Reson. Med.* 2023; 89:2186–2203.
- [22] Doneva M, Börnert P, Eggers H, Stehning C, S  n  gas J, Mertins A. Compressed sensing reconstruction for magnetic resonance parameter mapping. *Magn. Reson. Med.* 2010; 64:1114–1120.
- [23] Petzschner FH, Ponce IP, Blaimer M, Jakob PM, Breuer FA. Fast MR parameter mapping using k-t principal component analysis. *Magn. Reson. Med.* 2011; 66:706–716.
- [24] Huang C, Graff CG, Clarkson EW, Bilgin A, Altbach MI. T2 mapping from highly undersampled data by reconstruction of principal component coefficient maps using compressed sensing. *Magn. Reson. Med.* 2012; 67:1355–1366.
- [25] Velikina JV, Alexander AL, Samsonov A. Accelerating MR parameter mapping using sparsity-promoting regularization in parametric dimension. *Magn. Reson. Med.* 2013; 70:1263–1273.
- [26] Zhao B, Lu W, Hitchens TK, Lam F, Ho C, Liang ZP. Accelerated MR parameter mapping with low-rank and sparsity constraints. *Magn. Reson. Med.* 2015; 74:489–498.
- [27] Tamir JI, Uecker M, Chen W, Lai P, Alley MT, Vasanawala SS, Lustig M. T2 shuffling: Sharp, multicontrast, volumetric fast spin-echo imaging. *Magn. Reson. Med.* 2017; 77:180–195.
- [28] Zimmermann M, Abbas Z, Dzieciol K, Shah NJ. Accelerated parameter mapping of multiple-echo gradient-echo data using model-based iterative reconstruction. *IEEE Trans. Med. Imaging* 2017; 37:626–637.
- [29] Dong Z, Wang F, Reese TG, Bilgic B, Setsompop K. Echo planar time-resolved imaging with subspace reconstruction and optimized spatiotemporal encoding. *Magn. Reson. Med.* 2020; 84:2442–2455.

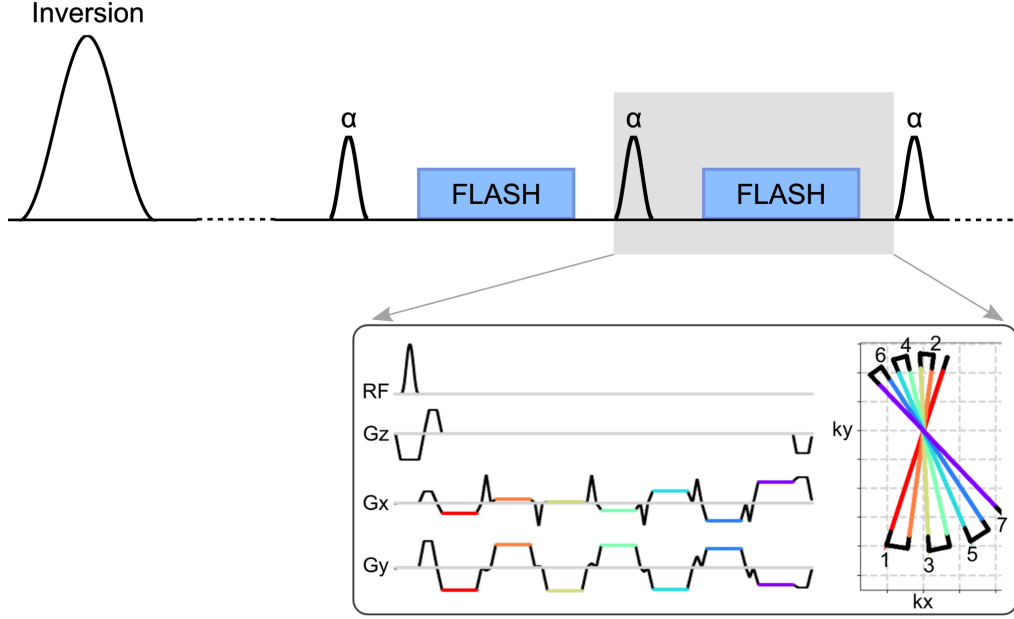
- [30] Wang X, Tan Z, Scholand N, Roeloffs V, Uecker M. Physics-based reconstruction methods for magnetic resonance imaging. *Philos. Trans. R. Soc. A* 2021; 379:20200196.
- [31] Sutton BP, Noll DC, Fessler JA. Fast, iterative image reconstruction for MRI in the presence of field inhomogeneities. *IEEE Trans. Med. Imag.* 2003; 22:178–188.
- [32] Block KT, Uecker M, Frahm J. Model-Based Iterative Reconstruction for Radial Fast Spin-Echo MRI. *IEEE Trans. Med. Imaging* 2009; 28:1759–1769.
- [33] Fessler JA. Model-based image reconstruction for MRI. *IEEE Signal Process. Mag.* 2010; 27:81–89.
- [34] Zhao B, Lam F, Liang Z. Model-Based MR Parameter Mapping With Sparsity Constraints: Parameter Estimation and Performance Bounds. *IEEE Trans. Med. Imaging* 2014; 33:1832–1844.
- [35] BenEliezer N, Sodickson DK, Shepherd T, Wiggins GC, Block KT. Accelerated and motion-robust in vivo T2 mapping from radially undersampled data using bloch-simulation-based iterative reconstruction. *Magn. Reson. Med.* 2016; 75:1346–1354.
- [36] Hilbert T, Sumpf TJ, Weiland E, Frahm J, Thiran JP, Meuli R, Kober T, Krueger G. Accelerated T2 mapping combining parallel MRI and model-based reconstruction: GRAPPATINI. *J. Magn. Reson. Imaging* 2018; 48:359–368.
- [37] Scholand N, Wang X, Roeloffs V, Rosenzweig S, Uecker M. Quantitative MRI by nonlinear inversion of the Bloch equations. *Magn. Reson. Med.* 2023; 90:520–538.
- [38] Tan Z, UnterbergBuchwald C, Blumenthal M, Scholand N, Schaten P, Holme C, Wang X, Raddatz D, Uecker M. Free-Breathing Liver Fat, R2* and B0 Field Mapping Using Multi-Echo Radial FLASH and Regularized Model-based Reconstruction. *IEEE Trans. Med. Imaging* 2023; 42:1374–1387.
- [39] Funai AK, Fessler JA, Yeo DT, Olafsson VT, Noll DC. Regularized field map estimation in MRI. *IEEE Trans. Med. Imaging* 2008; 27:1484–1494.
- [40] Wang X, Roeloffs V, Klosowski J, Tan Z, Voit D, Uecker M, Frahm J. Model-based T1 mapping with sparsity constraints using single-shot inversion-recovery radial FLASH. *Magn. Reson. Med.* 2018; 79:730–740.
- [41] Tan Z, Voit D, Kollmeier JM, Uecker M, Frahm J. Dynamic water/fat separation and inhomogeneity mapping adjoint estimation using undersampled triple-echo multi-spoke radial FLASH. *Magn. Reson. Med.* 2019; 82:1000–1011.

- [42] Winkelmann S, Schaeffter T, Koehler T, Eggers H, Doessel O. An optimal radial profile order based on the Golden Ratio for time-resolved MRI. *IEEE Trans. Med. Imag.* 2007; 26:68–76.
- [43] Yu H, Shimakawa A, McKenzie CA, Brodsky E, Brittain JH, Reeder SB. Multiecho water-fat separation and simultaneous R2* estimation with multifrequency fat spectrum modeling. *Magn. Reson. Med.* 2008; 60:1122–1134.
- [44] Stupic KF, Ainslie M, Boss MA, Charles C, Dienstfrey AM, Evelhoch JL, Finn P, Gimbutas Z, Gunter JL, Hill DL et al. A standard system phantom for magnetic resonance imaging. *Magn. Reson. Med.* 2021; 86:1194–1211.
- [45] Pruessmann KP, Weiger M, Scheidegger MB, Boesiger P. SENSE: sensitivity encoding for fast MRI. *Magn. Reson. Med.* 1999; 42:952–962.
- [46] Uecker M, Hohage T, Block KT, Frahm J. Image reconstruction by regularized nonlinear inversion-joint estimation of coil sensitivities and image content. *Magn. Reson. Med.* 2008; 60:674–682.
- [47] Uecker M, Ong F, Tamir JI, Bahri D, Virtue P, Cheng JY, Zhang T, Lustig M. Berkeley advanced reconstruction toolbox. In: *Proc. Intl. Soc. Mag. Reson. Med.*, Toronto, 2015. p. 2486.
- [48] Barral JK, Gudmundson E, Stikov N, EtezadiAmoli M, Stoica P, Nishimura DG. A robust methodology for in vivo T1 mapping. *Magn. Reson. Med.* 2010; 64:1057–1067.
- [49] Blumenthal M, Luo G, Schilling M, Holme HCM, Uecker M. Deep, deep learning with BART. *Magn. Reson. Med.* 2023; 89:678–693.
- [50] Rosenzweig S, Holme HCM, Uecker M. Simple auto-calibrated gradient delay estimation from few spokes using Radial Intersections (RING). *Magn. Reson. Med.* 2019; 81:1898–1906.
- [51] Huang F, Vijayakumar S, Li Y, Hertel S, Duensing GR. A software channel compression technique for faster reconstruction with many channels. *Magn. Reson. Imaging* 2008; 26:133–141.
- [52] Uecker M, Zhang S, Frahm J. Nonlinear inverse reconstruction for real-time MRI of the human heart using undersampled radial FLASH. *Magn. Reson. Med.* 2010; 63:1456–1462.
- [53] Wang X, Rosenzweig S, Roeloffs V, Blumenthal M, Scholand N, Tan Z, Holme HCM, UnterbergBuchwald C, Hinkel R, Uecker M. Free-breathing myocardial T1 mapping using inversion-recovery radial FLASH and motion-resolved model-based reconstruction. *Magn. Reson. Med.* 2023; 89:1368–1384.
- [54] Wajer FTAW, Pruessmann KP. Major speedup of reconstruction for sensitivity encoding with arbitrary trajectories. In: *Proc. Intl. Soc. Mag. Reson. Med.*, Glasgow, 2001. p. 0767.

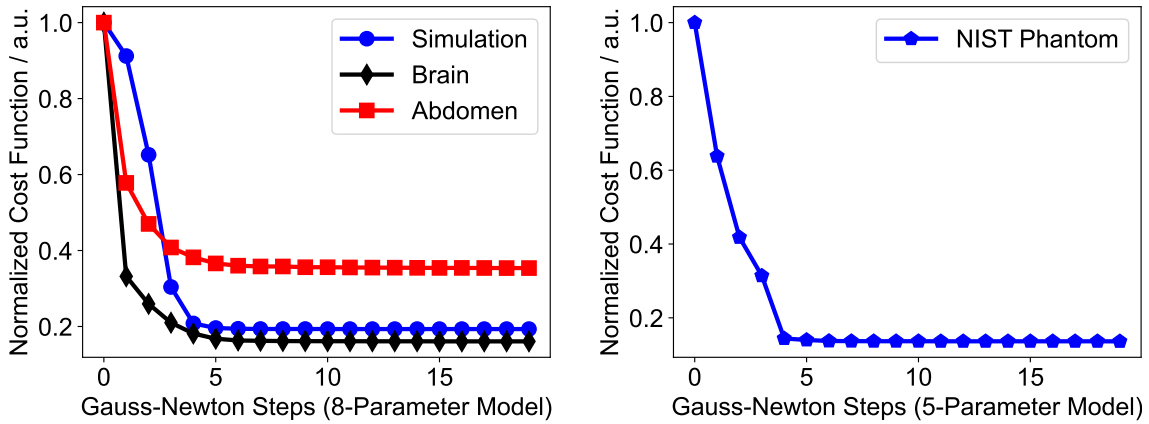
- [55] Sumpf T, Unterberger M. arrayshow: a guide to an open source matlab tool for complex MRI data analysis. In: Proc. Intl. Soc. Mag. Reson. Med., Salt Lake City, 2013. p. 2719.
- [56] Zimmermann M, Sommer Y, Abbas Z, Lewin A, OrosPeusquens AM, Yun SD, Shah NJ, Ramkiran S. QRAGE - Multi-Echo MPnRAGE and Model-Based Reconstruction for Quantitative MRI of Water Content, T1, T2* and Magnetic Susceptibility at 7T. In: Proc. Intl. Soc. Mag. Reson. Med., Toronto, 2023. p. 1091.
- [57] Heydari A, Ahmadi A, Kim TH, Bilgic B. Joint MAPLE: Accelerated joint T1 and T2* mapping with scan-specific self-supervised networks. Magn. Reson. Med. 2024; DOI: 10.1002/mrm.29989.
- [58] Mozes FE, Tunncliffe EM, Pavlides M, Robson MD. Influence of fat on liver T1 measurements using modified Look-Locker inversion recovery (MOLLI) methods at 3T. J. Magn. Reson. Imaging 2016; 44:105–111.
- [59] Rosenzweig S, Holme HCM, Wilke RN, Voit D, Frahm J, Uecker M. Simultaneous multi-slice MRI using cartesian and radial FLASH and regularized nonlinear inversion: SMS-NLINV. Magn. Reson. Med. 2018; 79:2057–2066.

Supporting Information File

Model-Based Reconstruction for Joint Estimation of T_1 , R_2^* and B_0 Field Maps Using Single-Shot Inversion-Recovery Multi-Echo Radial FLASH



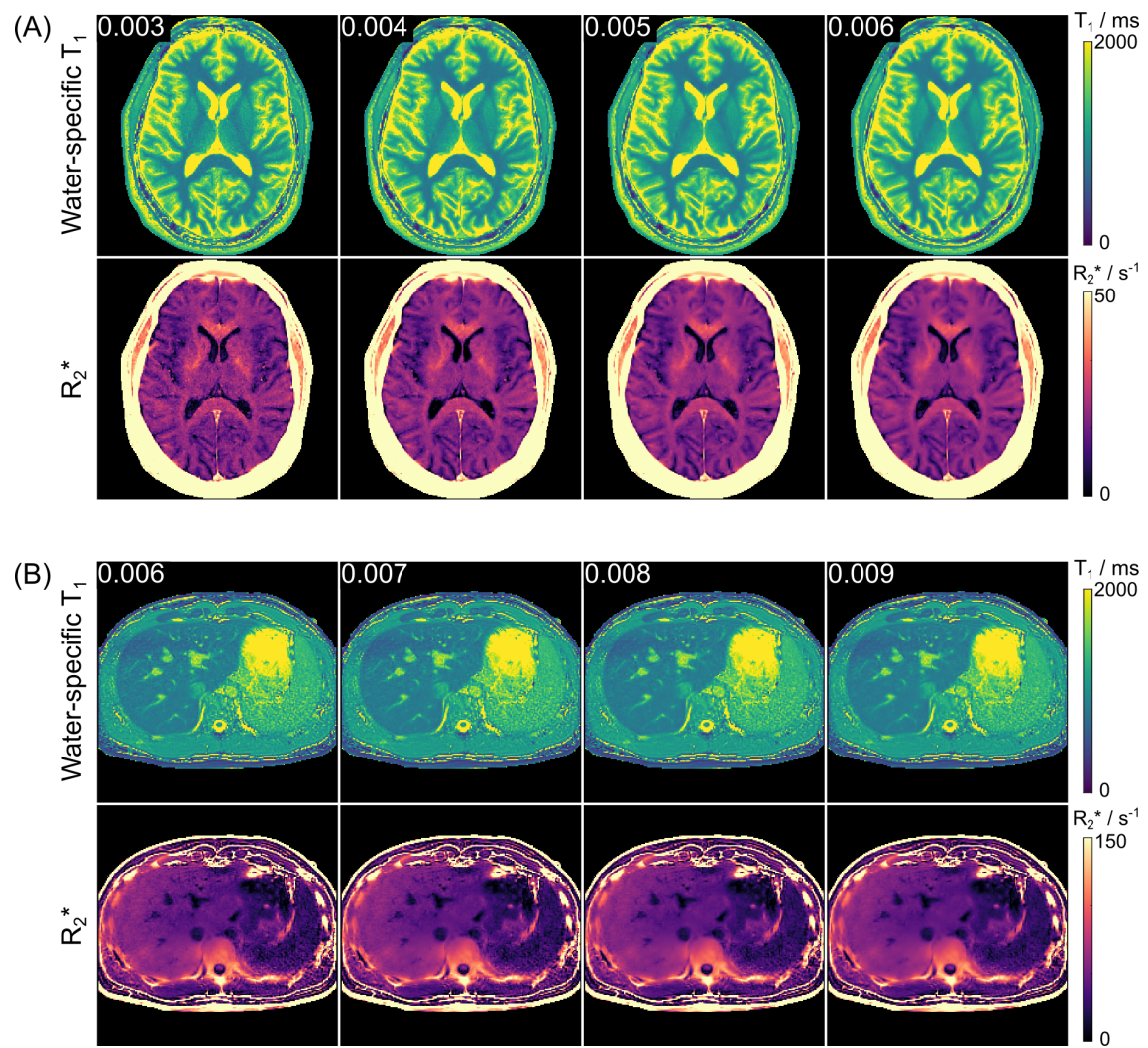
Supporting Information Figure S1. Schematic diagram of the single-shot inversion-recovery multi-echo radial FLASH sequence. The distribution of spokes is designed in a way that radial spokes from several TRs (e.g., 9) and all echoes are equally distributed in one k -space. Each k -space is then rotated by a small golden-angle during inversion recovery. Note that the blip gradients across echoes enable an efficient coverage of k -space.



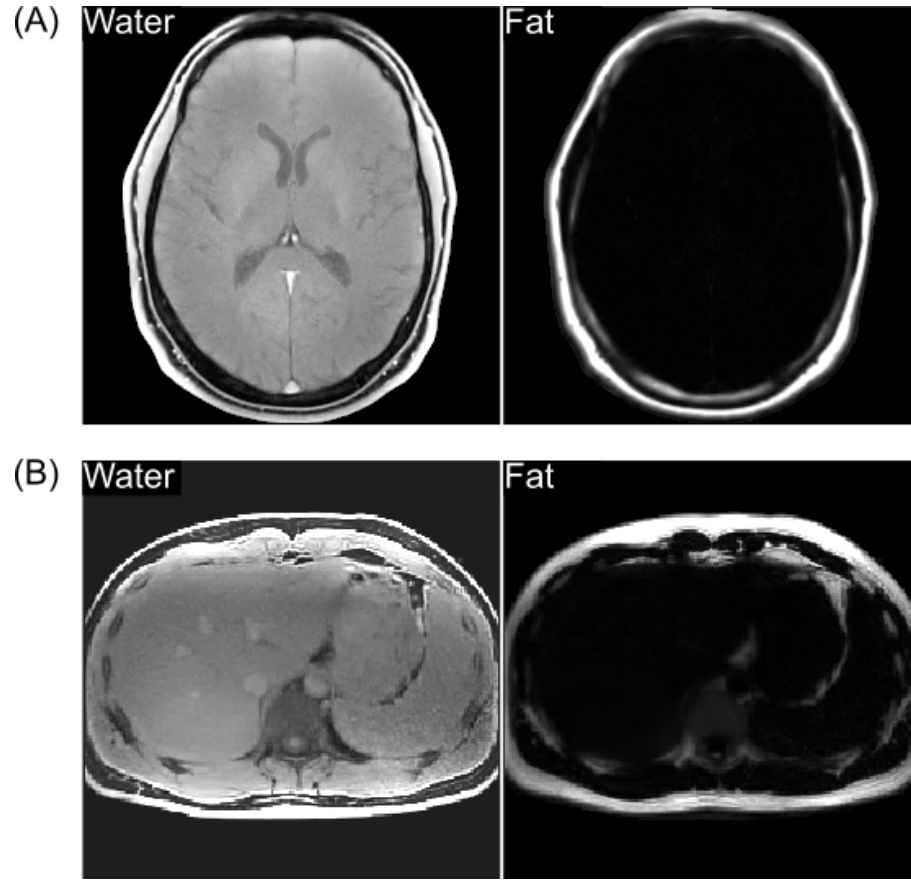
Supporting Information Figure S2. Normalized cost function (data fidelity term) as a function of Gauss-Newton steps for different data sets and for both (left) 8-parameter and (right) 5-parameter models.

Supporting Information Table S1. Acquisition parameters for IR multi-echo radial FLASH MRI of NIST phantom, human brain, and abdomen.

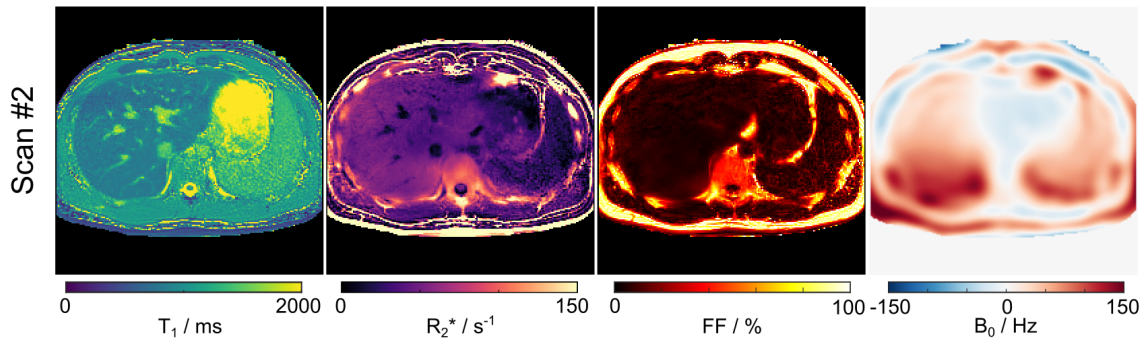
	Phantom / Brain	Abdomen
Field-of-view / mm^2	220×220 / 208×208	320×320
Image matrix	256×256	200×200
Resolution	0.86×0.86 / 0.81×0.81	1.6×1.6
Slice thickness / mm	5	6
Repetition time / ms	15.6	10.6
Number of echoes	7	7
Echo times / ms	2.36/4.26/6.16/8.06/9.96/11.90/13.80	1.49/2.61/3.73/4.85/5.97/7.09/8.21
Bandwidth / Hz pixel^{-1}	810	1320
Flip angle / degree	6	6
N_S (No. of TRs) per k -space frame	9	9
Total number of excitation	300	360
Total acquisition time / s	4	4



Supporting Information Figure S3. (A) Quantitative brain water-specific T_1 and R_2^* maps reconstructed with different regularization parameters. (B) The similar comparison for the abdominal study.



Supporting Information Figure S4. Model-based reconstructed water (W_{ss}) and fat (F_{ss}) images for (A) brain and (B) liver studies.



Supporting Information Figure S5. Model-based reconstructed liver water-specific T_1 , R_2^* , fat fraction and B_0 maps for the second scan.